The Inland Penetration of Atmospheric Rivers over Western North America: A Lagrangian Analysis

JONATHAN J. RUTZ

National Weather Service, Western Region Headquarters, Salt Lake City, Utah

W. JAMES STEENBURGH

University of Utah, Salt Lake City, Utah

F. MARTIN RALPH

Scripps Institute of Oceanography, La Jolla, California

(Manuscript received 9 September 2014, in final form 15 January 2015)

ABSTRACT

Although atmospheric rivers (ARs) typically weaken following landfall, those that penetrate inland can contribute to heavy precipitation and high-impact weather within the interior of western North America. In this paper, the authors examine the evolution of ARs over western North America using trajectories released at 950 and 700 hPa within cool-season ARs along the Pacific coast. These trajectories are classified as coastal decaying, inland penetrating, or interior penetrating based on whether they remain within an AR upon reaching selected transects over western North America. Interior-penetrating AR trajectories most frequently make landfall along the Oregon coast, but the greatest fraction of landfalling AR trajectories that eventually penetrate into the interior within an AR is found along the Baja Peninsula. In contrast, interior-penetrating AR trajectories rarely traverse the southern "high" Sierra. At landfall, interior-penetrating AR trajectories are associated with a more amplified flow pattern, more southwesterly (vs westerly) flow along the Pacific coast, and larger water vapor transport (qv). The larger initial qv of interior-penetrating AR trajectories is due primarily to larger initial water vapor q and wind speed v for those initiated at 950 and 700 hPa, respectively.

Inland- and interior-penetrating AR trajectories maintain large qv over the interior partially due to increases in v that offset decreases in q, particularly in the vicinity of topographical barriers. Therefore, synoptic conditions and trajectory pathways favoring larger initial qv at the coast, limited water vapor depletion by orographic precipitation, and increases in v over the interior are keys to differentiating interior-penetrating from coastal-decaying ARs.

1. Introduction

Atmospheric rivers (ARs) are long and narrow regions of intense vertically integrated water vapor transport (IVT; Newell et al. 1992; Newell and Zhu 1994; Zhu and Newell 1998) that frequently produce heavy precipitation when they intersect high mountain barriers (Neiman et al. 2002; Ralph et al. 2004, 2005, 2013). During the cool season, these conditions are common along the Pacific coast, where many cases of heavy AR-related rainfall and flooding have been documented (Ralph et al. 2006, 2011; Neiman et al. 2008, 2011). ARs have also been linked to extreme precipitation and flooding over western Europe (Stohl et al. 2008; Lavers et al. 2011) and the eastern United States (Moore et al. 2012). The penetration of ARs into interior western North America is less frequent, but can likewise produce heavy precipitation (Lackmann et al. 1998; Rigby 1998; Bernhardt 2006; Neiman et al. 2013, 2014; Rutz et al. 2014; Hughes et al. 2014).

Recent studies have attempted to quantify the fraction of precipitation attributable to ARs over the western United States. To facilitate this, some authors have identified ARs following Ralph et al. (2004) as contiguous regions $\geq$2000 km in length and $\leq$1000 km in width with integrated water vapor (IWV) $\geq$20 mm. Dettinger et al. (2011) used

Corresponding author address: Jonathan J. Rutz, National Weather Service, Western Region Headquarters, Room 1235, 125 South State St., Salt Lake City, UT 84138.
E-mail: jonathan.rutz@noaa.gov

DOI: 10.1175/MWR-D-14-00288.1

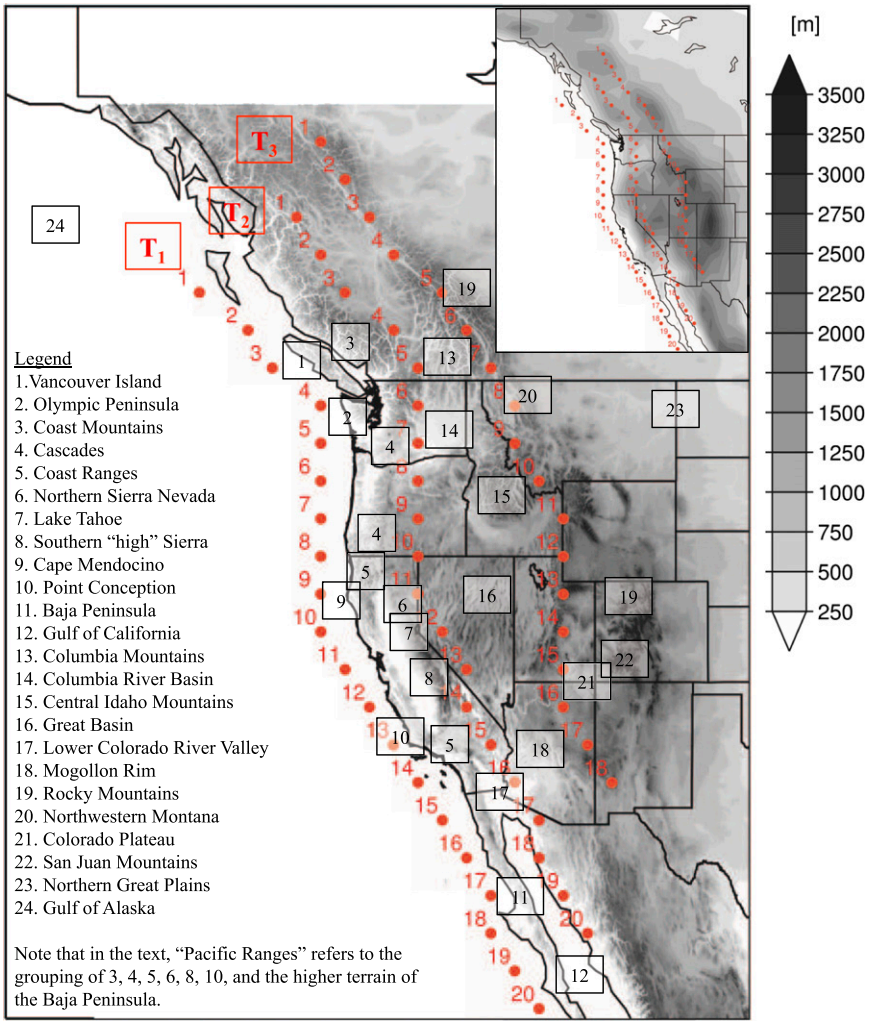

FIG. 1. Surface elevation (30 arc s) over the western United States, in grayscale shading. Points along transects T_1, T_2, and T_3 are numbered in red. Legend indicates geographic terms at numbered locations. Inset figure shows ERA-Interim (1.5°) surface elevation.

this method to construct an 11-yr climatology of ARs and found that 20%–50% of total cool-season precipitation at most sites in California, Oregon, and Washington fell on the day of or day after an AR landfall along the Pacific coast from 32.5° to 52.5°N. Farther inland, lower fractions of cool-season precipitation were attributed to ARs, particularly over the southwestern United States (<15%), although Rutz and Steenburgh (2012) found higher fractions (15%–40%) over the Southwest by extending the analysis to include ARs crossing the Baja Peninsula (24°–32.5°N).

Rutz et al. (2014) showed that over much of the western United States, IVT is more useful than IWV for exploring the relationship between cool-season ARs and precipitation, and objectively identified ARs as contiguous regions ≥2000 km in length with IVT ≥250 kg m^{-1} s^{-1}. Using this approach, the AR frequency (i.e., the percentage of ERA-Interim reanalyses with an AR present) is largest (>16%) along the Oregon and Washington coasts and decreases southward along the California coast and eastward over the Pacific Ranges (geographic features identified in Fig. 1). Over the interior, the AR frequency is largest along a relatively low-elevation corridor extending from the Oregon and Washington coasts eastward across the Columbia River basin and through the northern U.S. Rockies, whereas it is smallest (<3%) over the southwestern United States, the eastern Great Basin, and the central Rockies. Rutz et al. (2014) also found that the fraction of top-decile 24-h precipitation events (top-decile fraction) attributable to ARs is greatest (>0.55) along the U.S. West Coast, particularly north of San Francisco, and smallest (<0.15) from just to the east (lee) of the southern "high" Sierra across the central Great Basin to Colorado and

Wyoming. Over the northwest and southwest interior, the top-decile fraction ranges from 0.15 to 0.55 and exhibits large mesoscale variability.

Wernli (1997) used a Lagrangian-based analysis to examine coherent flow structures within a North Atlantic cyclone, including the movement of trajectories through the concomitant AR-like water vapor flux maximum. Subsequently, Stohl et al. (2008) showed that heavy precipitation along the Norwegian coast is often associated with trajectories that pass through ARs. The specific humidity of these trajectories typically increases over a broad swath of the Atlantic Ocean. More generally, the development and decay of extratropical and sometimes tropical cyclones can influence water vapor fluxes into and within ARs, offsetting losses due to precipitation (Sodemann and Stohl 2013; Cordeira et al. 2013). Knippertz and Wernli (2010) developed a method to identify Northern Hemisphere trajectories originating in the tropics (south of 20°N) and obtaining water vapor fluxes $\geq 100\,\mathrm{g\,kg^{-1}\,m\,s^{-1}}$ north of 35°N, referring to these as tropical moisture export (TME) trajectories. Subsequently, Knippertz et al. (2013) showed that outbreaks of TME trajectories over the northeastern Pacific were strongly related to the ARs identified by Dettinger et al. (2011) along the U.S. West Coast.

It is not well understood what factors differentiate the majority of ARs that decay along and upstream of the Pacific Ranges and the minority that penetrate into interior western North America. In a Lagrangian framework, the maintenance or decay of ARs is related to changes in water vapor flux (i.e., specific humidity and wind) following the flow. Therefore, in this study, we initiate low- (950 hPa) and midlevel (700 hPa) 72-h forward trajectories within ARs approaching the Pacific coast (24°–52.5°N) to explore the processes contributing to AR maintenance or decay over western North America. Of particular interest is identifying the factors that differentiate coastal-decaying ARs from those that penetrate into the western interior. Because ARs can produce heavy precipitation, the results have broad applications in weather, hydrologic, and climate research and forecasting. Section 2 describes the data and methods used. Sections 3–6 examine the pathways, initial characteristics, displacements, and water vapor flux tendencies of coastal-decaying, inland-, and interior-penetrating trajectories. Section 7 presents composite analyses that highlight differences in the synoptic environment of these three trajectory classifications. Section 8 presents an idealized schematic that integrates key findings from this study and Rutz et al. (2014) concerning the inland penetration of ARs over western North America. Finally, section 9 provides a summary and suggestions for future work.

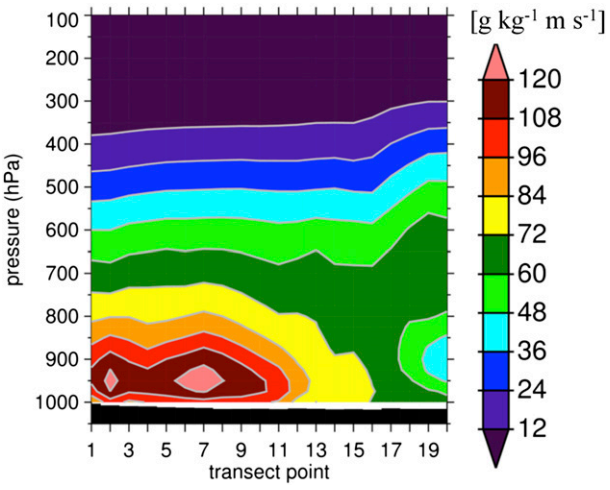

FIG. 2. Cross section of mean cool-season water vapor flux when an AR is identified at T_1 grid points. Mean surface pressure is shaded in black.

2. Data and methods

Trajectories are calculated using data from the ERA-Interim (Dee et al. 2011), which is based on a version of the European Centre for Medium-Range Weather Forecasts (ECMWF) Integrated Forecast System (IFS) with 60 vertical levels (extending to 0.1 hPa), T255 triangular truncation for dynamical fields, and a reduced Gaussian grid with ~80-km spacing for surface and other gridpoint fields (Simmons et al. 2007; Uppala et al. 2008; Berrisford et al. 2009). The ~80-km Gaussian grid spacing provides a reasonable estimate of the effective grid spacing of the ERA-Interim in physical space (Kanamitsu 1989). All data are obtained from the ECMWF data server on a 1.5° latitude × 1.5° longitude grid with 6-h temporal resolution. These data are then interpolated to 1-h resolution for the 72-h trajectory calculations, which are based on the zonal, meridional, and vertical wind components and use trilinear interpolation to obtain atmospheric data at each subsequent trajectory location.

At each 6-h ERA-Interim analysis time during the cool-season months (November–April) from November 1988 to April 2011, ARs are identified following Rutz et al. (2014) as contiguous Eulerian features with length $\geq 2000\,\mathrm{km}$ and vertically IVT $\geq 250\,\mathrm{kg\,m^{-1}\,s^{-1}}$. Trajectories are initiated at 950 and 700 hPa whenever an AR is present at a grid point along a transect, T_1, ~100–200 km west of the Pacific coast (Fig. 1). We select 950 and 700 hPa for trajectory initiation because the level of maximum mean water vapor flux during AR landfall is ~950 hPa north of the central Baja Peninsula (i.e., T_1 grid points 1–16, Fig. 2), whereas it is ~700 hPa during AR landfall along the southern Baja Peninsula (i.e., T_1 grid points 17–20, Fig. 2). In addition, 700 hPa (~3000 m) is

near or just below the crest of many western North American mountain barriers.

We then classify these AR trajectories based on their pathways and characteristics if and when they reach two selected transects over the interior western United States. The first, T_2, lies immediately east of the Pacific Ranges, which encompass the Canadian Coast Mountains, the Cascades, the Sierra Nevada, the U.S. Coast Ranges, and the higher topography of Southern California and the Baja Peninsula (see Fig. 1). These ranges typically represent the first major topographic barriers encountered by landfalling ARs (Fig. 1). The second, T_3, extends from the northern Rocky Mountains to the Mogollon Rim along ranges that typically represent the second major topographic barriers encountered by landfalling ARs.

Trajectories that do not reach T_2 during their 72-h integration period are removed from the analysis. Trajectories that reach T_2 are divided into three subsets. Those not within an AR upon reaching T_2 are classified as *coastal-decaying AR trajectories*. Those that reach T_2 but not T_3 within an AR are classified as *inland-penetrating AR trajectories*. Those that reach T_3 within an AR are classified as *interior-penetrating AR trajectories*.

Of the trajectories no longer within an AR upon reaching T_2 or T_3, some fraction may have simply exited the AR horizontally due to flow blocking or divergence, but in most instances, this reflects AR decay due to water vapor depletion, as suggested by the rapid decrease in AR frequency as one moves inland (e.g., Rutz et al. 2014).

Spatial analyses of mean trajectory characteristics (e.g., water vapor flux, specific humidity, and wind speed) are created by defining a 1.0° latitude × 1.0° longitude grid over the western United States and Canada. At each 1-h time step, we record the characteristics of each trajectory, which is then used to calculate the mean within each grid box. If a trajectory resides within one grid box for more than one time step, an average of its characteristics over all steps within that grid cell is taken and recorded as one value. This prevents overall statistics from being skewed by slow-moving trajectories.

3. Trajectory pathways

Coastal-decaying 950-hPa AR trajectories are widely distributed over the western United States and southwestern Canada and are characterized by rapidly decreasing water vapor flux (qv, where q is the specific humidity and v is the horizontal wind speed) upstream and over the Pacific Ranges (Fig. 3a). The greatest frequency of such trajectories (i.e., the number passing through a given 1.0° × 1.0° grid cell) extends from the Pacific coast into the interior northwestern United States and southwestern Canada (Fig. 3d). The trajectory frequency decreases toward the south, and is least over the southwestern United States and Mexico.

The distribution of inland-penetrating 950-hPa AR trajectories is strongly influenced by the Pacific Ranges, as these trajectories must generally maintain large qv until reaching T_2 (Figs. 3b,e). The distribution of interior-penetrating 950-hPa AR trajectories are additionally influenced by the rugged interior topography, as these must also maintain large qv until reaching T_3 (Figs. 3c,f). The frequencies of inland- and interior-penetrating AR trajectories are greatest along a corridor extending from the Oregon and Washington coasts eastward across the Columbia River basin and the northern U.S. Rockies just south of the U.S.–Canada border. Secondary maxima extend along the relatively low-elevation corridor north of the Canadian Coast Mountains and from the Baja Peninsula into the southwestern United States. In contrast, few inland- and interior-penetrating AR trajectories are found southwest, over, and northeast of the high Sierra, which contribute strongly to AR decay (Rutz et al. 2014). A secondary minimum lies over and downstream of Vancouver Island and the high terrain of the Coast Mountains.

The distributions of 700-hPa AR trajectories are similar to those initiated at 950-hPa, but are generally characterized by less topographic influence, smaller water vapor fluxes, and a more westerly flow direction (cf. Figs. 3 and 4). The frequency of inland- and interior-penetrating AR trajectories is again largest along a corridor extending from the Oregon and Washington coasts eastward across the Columbia River basin and the northern United States and southern Canadian Rockies, but this corridor is broader than for 950-hPa AR trajectories. The frequency of inland- and interior-penetrating AR trajectories is smallest across the high Sierra, but this minimum is less dramatic than for the 950-hPa AR trajectories. In addition, the corridor of maximum trajectory frequencies over the northwestern United States (and to a lesser extent, the region of minimum frequencies downstream of the high Sierra) features a more zonal orientation than at 950 hPa, reflecting the dominant flow direction at this level. Overall, there are more inland- and interior-penetrating AR trajectories initiated at 700 than at 950 hPa, which is likely related to lower-level trajectories experiencing greater horizontal displacement (e.g., blocking and deflection), increasing the chances that they will exit an AR prior to reaching T_2.

Overall, the distributions of AR trajectories, particularly those initiated at 950 hPa, highlight three distinct pathways along which trajectories remain AR-related into the interior. The first pathway extends from the

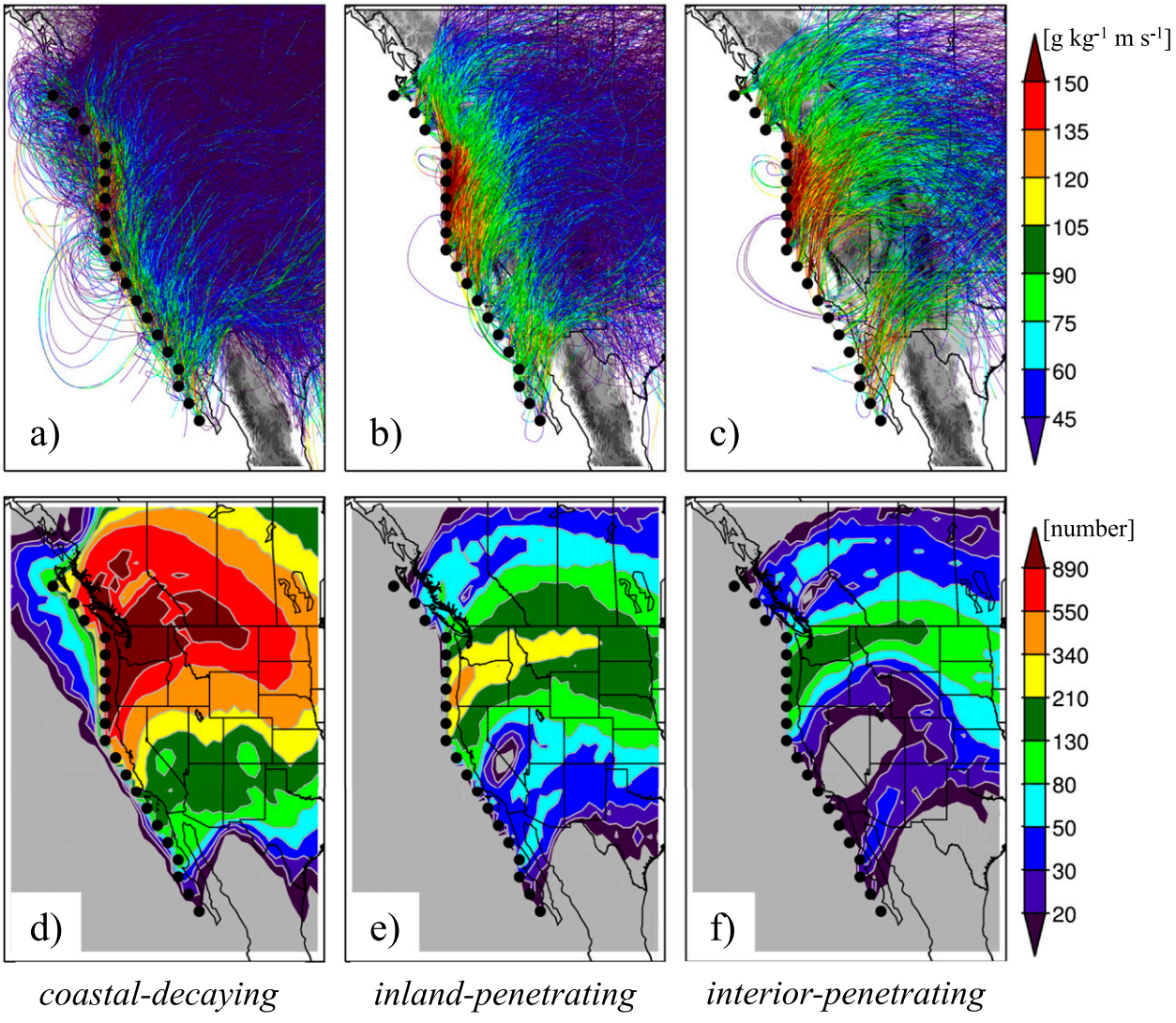

FIG. 3. (a) Coastal-decaying, (b) inland-penetrating, and (c) interior-penetrating AR trajectories colored by water vapor flux (scale at right). (d)–(f) As in (a)–(c), but for trajectory count. Black circles indicate T_1 grid points.

U.S. West Coast north of Cape Mendocino (~40.5°N) across the Columbia River basin, over the northern U.S. Rockies, and into the northern Great Plains. The second pathway lies north of the Coast Mountains of southwest Canada and extends through the relatively low gap north of the Columbia Mountains and Canadian Rockies. The third pathway extends from the Baja Peninsula into the southwestern United States. In contrast, a dearth of inland-and interior-penetrating AR trajectories exists from the central and Southern California coast [centered roughly on Point Conception (~35.5°N)] northeastward across the high Sierra and into the Great Basin. The AR trajectories making landfall along this stretch of coast rarely remain AR related upon reaching T_3 and, when they do, typically circumscribe the northern or southern flanks of the high Sierra. Overall, these results are in good agreement with those of Rutz et al. (2014), who identified two preferred pathways of AR penetration into the interior western United States, located north and south of the high Sierra (their analysis did not extend into southwestern Canada).

4. Trajectory characteristics at initiation

The frequency of 950- and 700-hPa AR trajectories initiated along T_1 and reaching T_2 is greatest west of Oregon (point 7) with a long tail to lower values west of the Baja Peninsula (Figs. 5a,b). The number of 950-hPa AR trajectories that can ultimately be classified as inland or interior penetrating (the latter represents

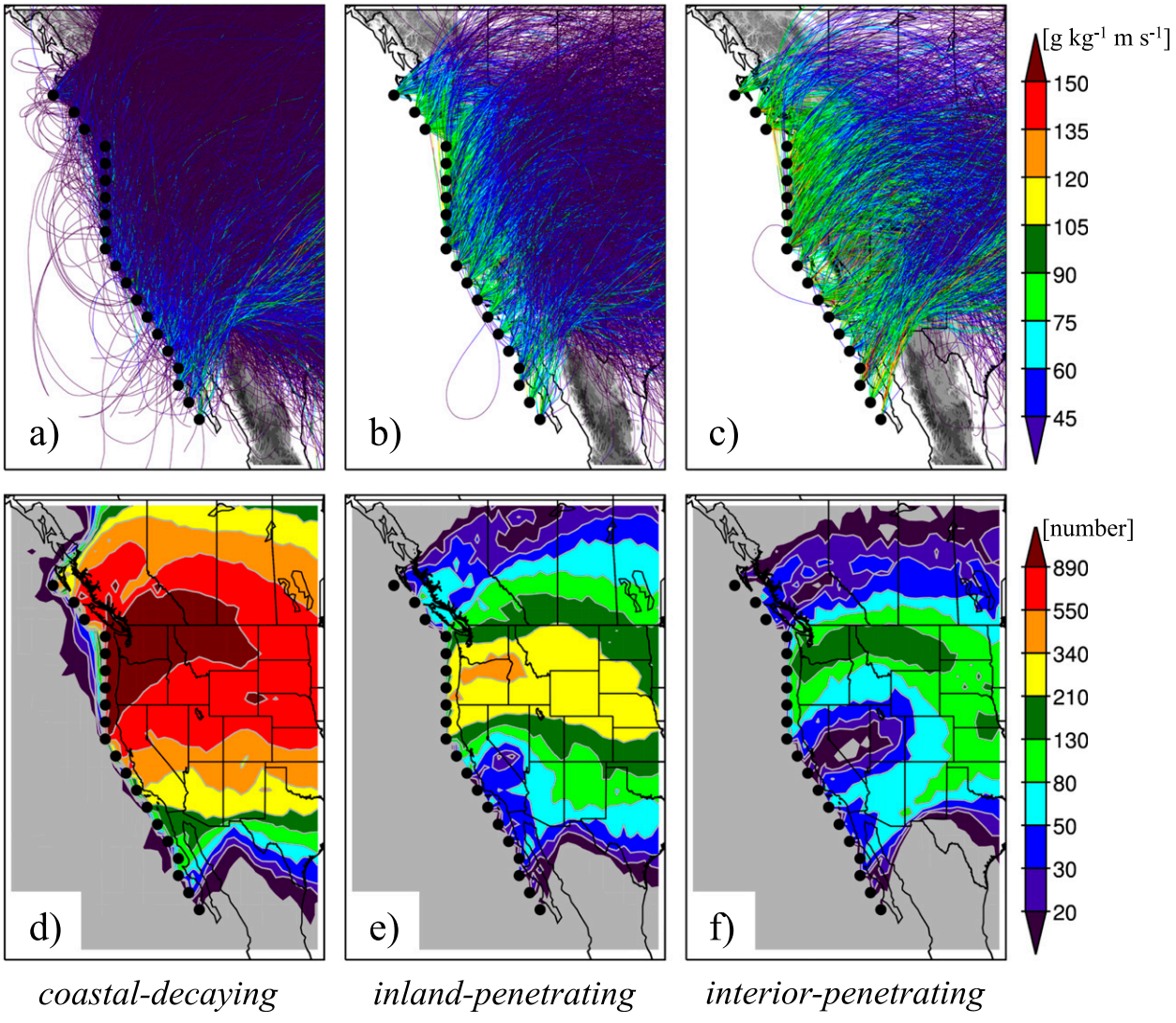

FIG. 4. As in Fig. 3, but for 700-hPa AR trajectories.

a subset of the former) is largest (~300) along the coasts of southern Oregon and Northern California [points 7–10 (Fig. 5a)]. However, the percentage of 950-hPa AR trajectories that become inland or interior penetrating is highest along the coasts of Southern California and the Baja Peninsula (points 14–20). The AR trajectories from 700 hPa exhibit similar fates, though with a greater fraction of those initiated along the Baja Peninsula becoming inland penetrating, perhaps because the ~700-hPa maximum in AR-related water vapor flux over this region lies above many of the topographical barriers encountered before reaching the Colorado Rockies (cf. Figs. 2 and 5b). Thus, although the number of inland-and interior-penetrating AR trajectories is highest along the coasts of southern Oregon and Northern California, trajectories associated with ARs approaching the coasts of Southern California and the Baja Peninsula are more likely to maintain AR characteristics as they penetrate inland. A local minimum in the fraction of interior-penetrating AR trajectories is found at points 11 and 12. This region is located west and southwest of the high Sierra, which strongly contribute to AR decay [see also Rutz et al. (2014)] and frequently prevent the penetration of AR trajectories into the interior (see also Fig. 3).

An important difference between coastal-decaying and interior-penetrating AR trajectories is the intensity of qv near the Pacific coast (i.e., at T_1 grid points). For those initiated at 950 hPa, the median (and general distribution) of qv for interior-penetrating AR trajectories is larger than that of coastal-decaying AR trajectories at all points except 18–20 (Fig. 6a). The difference in qv is largest west of the high Sierra (points 11 and 12), where

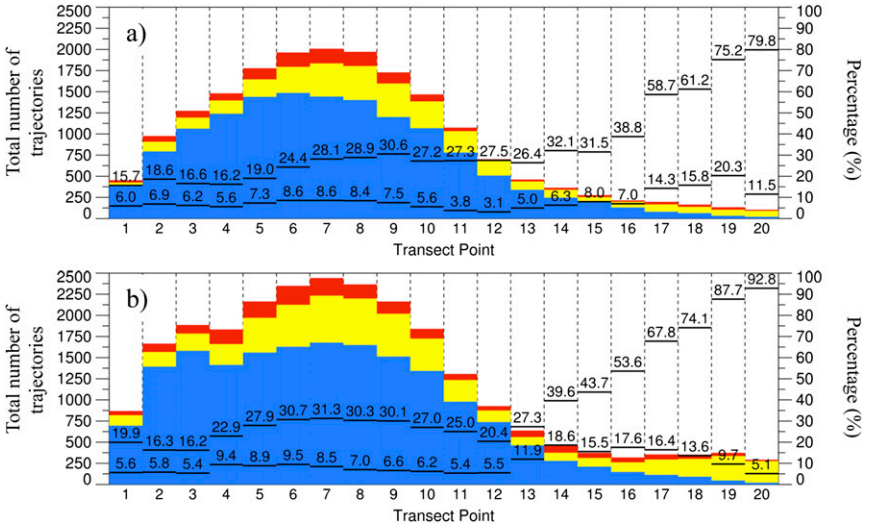

FIG. 5. (a) Number of coastal-decaying (blue), inland-penetrating (yellow), and interior-penetrating (red) 950-hPa AR trajectories initiated from T_1 grid points (left axis corresponds to the total of all three). Percentage of trajectories that are inland penetrating (upper series of black horizontal lines and numbers) and interior penetrating (lower series of black horizontal lines and numbers), with right axis corresponding to these percentages. (b) As in (a), but for 700-hPa AR trajectories.

the fraction of interior-penetrating AR trajectories is smallest. Here, very large values of initial qv are typically required for trajectories to remain AR related upon reaching T_3.

The median (and general distribution) of qv for interior-penetrating 700-hPa AR trajectories is larger than that of coastal-decaying AR trajectories at all T_1 grid points, including those upstream of the Baja Peninsula where the contrast in qv between interior-penetrating and coastal-decaying 950-hPa AR trajectories was not large (Fig. 7a). This distribution of qv suggests that for ARs making landfall along the Baja Peninsula, unusually large qv at midlevel elevations (700 hPa) may be more indicative of an AR that could potentially penetrate into the interior than unusually large qv at lower levels (950 hPa). Knippertz and Martin (2007) provide an example of such an event.

Breaking qv into specific humidity q and wind speed v, we find that the larger initial qv of interior-penetrating 950-hPa AR trajectories at points 1–17 is due primarily to a larger q, whereas v is often only slightly larger or even smaller than that of coastal-decaying AR trajectories (cf. Figs. 6b,c). In contrast, the larger initial qv of interior-penetrating 700-hPa AR trajectories is primarily due to a larger v (cf. Figs. 7b,c). These results suggest that anomalously large low-level (950 hPa) moisture and midlevel (700 hPa) wind speed are two key predictors of ARs with the potential to penetrate into the interior.

5. Trajectory displacements

Analyses of the displacements from the initial latitude and pressure help to further elucidate the three-dimensional pathways taken by AR trajectories as they move into the interior. We focus on 950-hPa AR trajectories, as the displacements in latitude and pressure of 700-hPa AR trajectories are somewhat less dramatic. The AR trajectories initiated at 950 hPa generally move in a broad, anticyclonic pattern over the northwestern United States and southwestern Canada, with small mean poleward displacements (2°–4°) from their original latitude (φ) as they move inland and a tendency to move equatorward east of the continental divide (Fig. 8, see also Fig. 3). There is little difference in the pattern and displacement of coastal-decaying, inland-penetrating, and interior-penetrating AR trajectories. In contrast, AR trajectories initiated west of Southern California and the Baja Peninsula generally move strongly north-northeastward, with inland- and interior-penetrating AR trajectories featuring larger mean poleward displacements (>6°) over the Colorado Plateau and adjoining Rocky Mountain region than coastal-decaying AR trajectories. The AR trajectories moving across Southern California and the northern Baja Peninsula generally exhibit weak cyclonic curvature, whereas those moving across the southern Baja Peninsula often exhibit weak anticyclonic curvature.

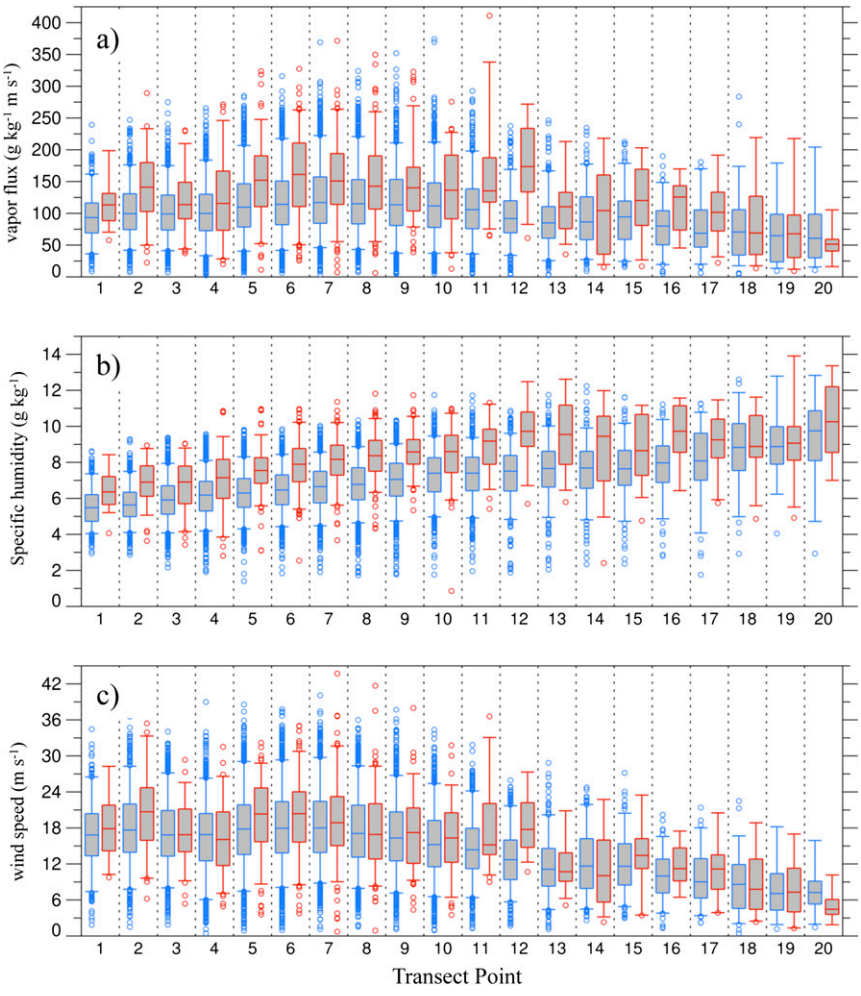

FIG. 6. (a) Box-and-whisker plot of initial water vapor flux (qv) at T_1 grid points for coastal-decaying (blue) and interior-penetrating (red) 950-hPa AR trajectories. Gray-shaded boxes indicate the interquartile range. Horizontal line within gray-shaded boxes indicates the median, and horizontal lines outside of boxes indicate the 5th and 95th percentiles. Circles indicate values below the 5th and above the 95th percentiles. (b) As in (a), but for specific humidity q. (c) As in (a), but for wind v.

Owing to the elevated terrain of the western United States, the initially low-level (950 hPa) AR trajectories generally experience ascent and a decrease in mean pressure as they move inland (Figs. 9a–c). Mean 1-h rates of ascent (i.e., $\overline{\Delta p_{1h}} < 0$) are generally largest over and west (upstream) of major mountain barriers (Figs. 9d,e), although such terrain-induced effects are not fully resolved by the ERA-Interim. For coastal-decaying AR trajectories, mean rates of ascent are largest over the Pacific Ranges of southwestern Canada and the northwestern United States, including Northern California (Fig. 9d). For inland- and interior-penetrating AR trajectories, topographic barriers in northern Idaho, central Arizona, and southwestern Colorado also produce large rates of ascent (Figs. 9e,f). Strong mean descent rates (i.e., $\overline{\Delta p_{1h}} > 0$) are found east (downstream) of the northern United States and southern Canadian Rockies, as well as the southern Rockies of Colorado and New Mexico. The magnitudes of displacement and rate of ascent/descent are larger for inland-penetrating than coastal-decaying AR trajectories, and largest for interior-penetrating AR trajectories.

6. Changes in water vapor flux

The mean qv ($\overline{qv}$) of interior-penetrating 950-hPa AR trajectories is larger than that of coastal-decaying AR trajectories as they approach the coast (along T_1, as shown in Fig. 10a) and over the interior (Figs. 10a–c). For interior-penetrating 950-hPa AR trajectories, $\overline{qv}$

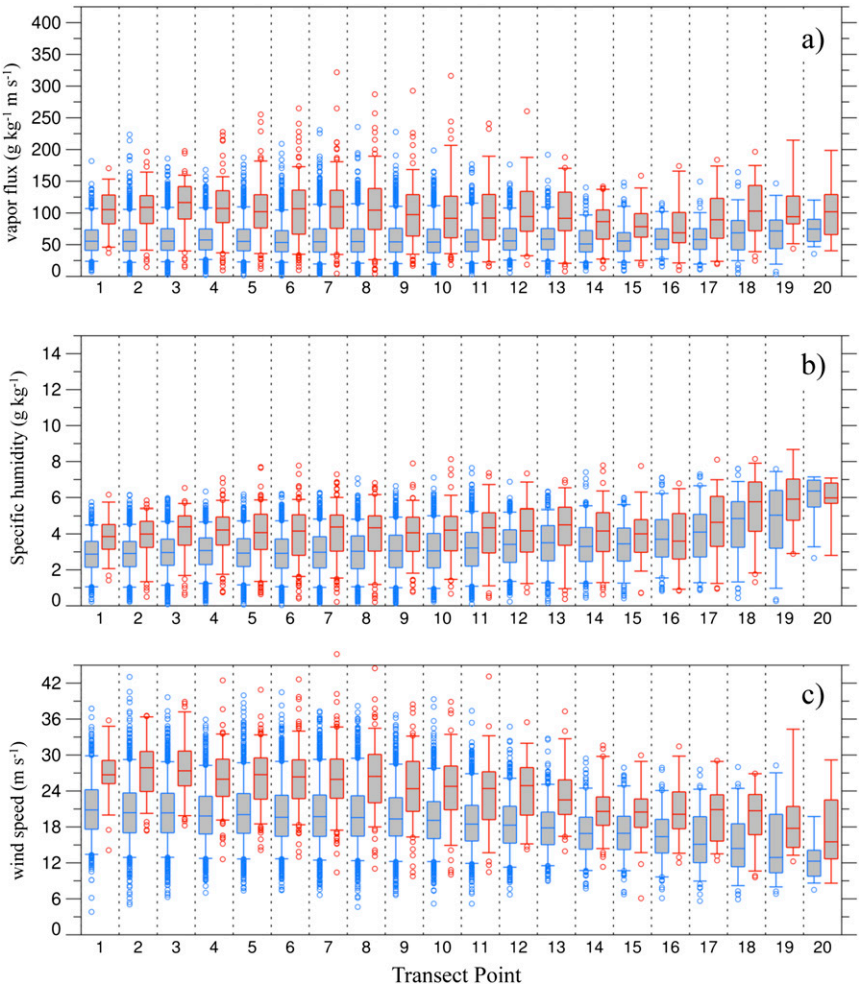

FIG. 7. As in Fig. 6, but for 700-hPa AR trajectories.

generally decreases from west to east over the interior, but larger values are found over the lower Colorado River valley, the northern Great Basin, and the corridor extending from the Oregon and Washington coasts eastward across the Columbia River basin and the northern United States and southern Canadian Rockies (Fig. 10c).

The mean q ($\overline{q}$) of 950-hPa AR trajectories is largest west of the Pacific Ranges and Mogollon Rim, decreases from west to east over the interior, and is smallest over and east of the Rocky Mountains (Figs. 10d–f). Over the interior, the $\overline{q}$ of interior-penetrating 950-hPa AR trajectories is $\sim$1 g kg^{-1} larger than that of inland-penetrating AR trajectories and $\sim$2 g kg^{-1} larger than that of coastal-decaying AR trajectories, with some regional variation (cf. Figs. 10d–f).

The mean v ($\overline{v}$) of 950-hPa AR trajectories is generally largest east of the Pacific Ranges and over the northern half of the interior, although it is also large for interior-penetrating AR trajectories over the Colorado Plateau (Figs. 10g–i). The $\overline{v}$ of interior-penetrating 950-hPa AR trajectories is much larger than that of coastal-decaying AR trajectories, particularly over the northern interior (cf. Figs. 10g–i).

To better differentiate between the characteristics of coastal-decaying, inland-, and interior-penetrating AR trajectories, we analyze relative changes in qv, q, and v along these trajectories. Specifically, we calculate the 1-h relative water vapor flux change (Δqv_{1h}) along the trajectory as

$$\Delta qv_{1h} = \frac{qv_t - qv_{t-1}}{qv_{t-1}} \times 100\%, \qquad (1)$$

where qv_t and qv_{t-1} are the water vapor flux at the current and previous 1-h time step, respectively. Similarly, the net relative water vapor flux change (Δqv_{net}) along the trajectory is calculated as

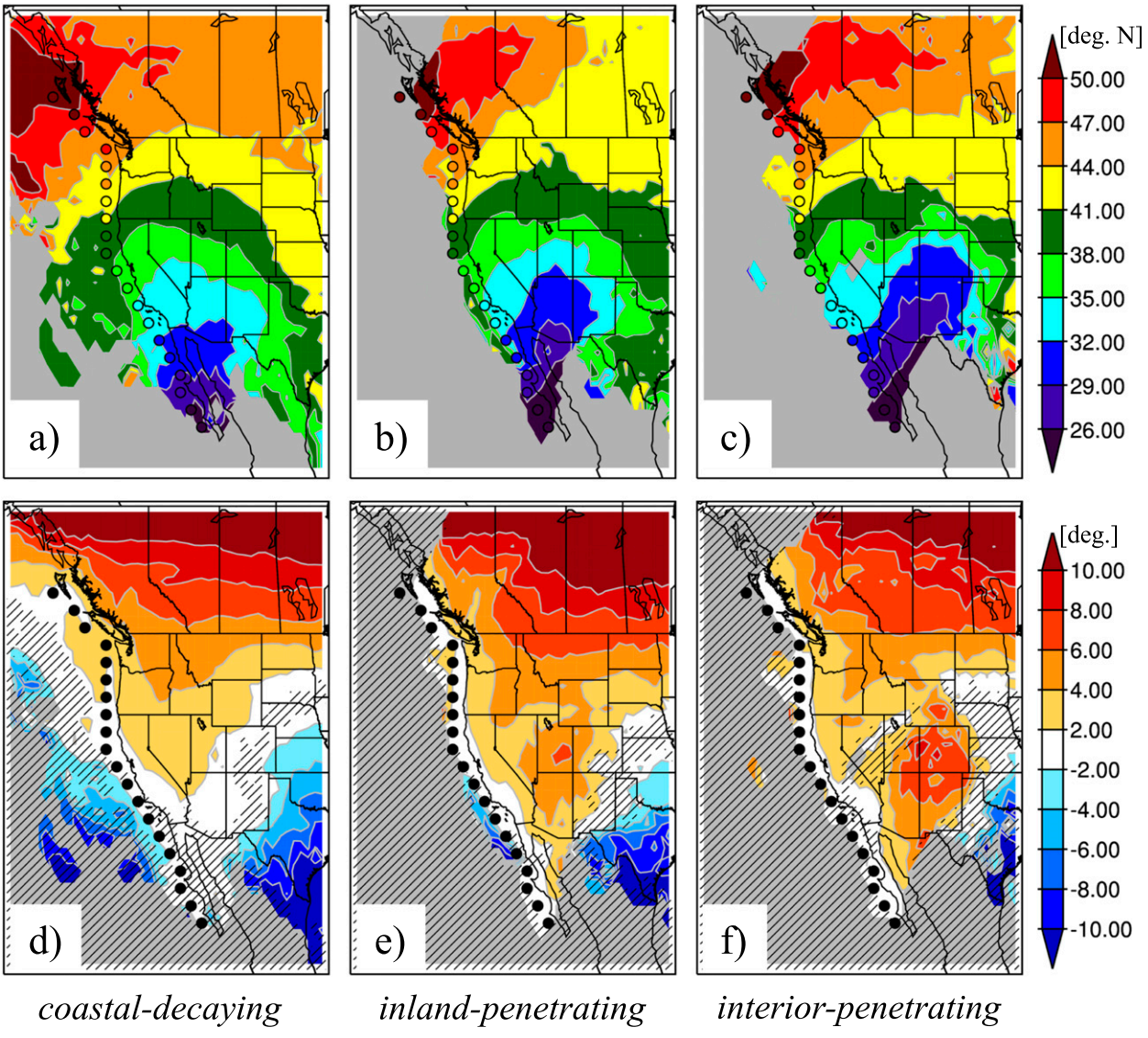

FIG. 8. (a)–(c) Spatial analysis of mean initial trajectory latitude ($\overline{\phi}$) for (a) coastal-decaying, (b) inland-penetrating, and (c) interior-penetrating 950-hPa AR trajectories. (d)–(f) As in (a)–(c), but for the mean net change in latitude, $\overline{\Delta\phi_{\text{net}}}$, integrated over time since trajectory initiation. Colored circles in (a)–(c) indicate latitude of T_1 grid points. Gray shading indicates no data and stippling indicates that results are not significant at the 95% confidence level following the Student's *t* test.

$$\Delta qv_{\text{net}} = \frac{qv_t - qv_0}{qv_0} \times 100\%, \qquad (2)$$

where qv_0 is the water vapor flux at trajectory initiation. The 1-h and net relative change in water vapor and wind speed are calculated in the same way. We stress that this analysis considers relative changes and not changes in the magnitude of these variables.

Along the coast, the mean 1-h relative water vapor flux change ($\overline{\Delta qv_{1h}}$) of 950-hPa AR trajectories is strongly negative ($<-10\%\ h^{-1}$) north of the Olympic Peninsula and less negative farther south (Figs. 11a–c). Over the interior, $\overline{\Delta qv_{1h}}$ is most strongly negative along the Idaho–Oregon border ($<-8\%\ h^{-1}$), in northwest Utah ($<-6\%\ h^{-1}$), and in western Colorado ($<-6\%\ h^{-1}$), and is less negative elsewhere. Coastal-decaying 950-hPa AR trajectories also exhibit negative $\overline{\Delta qv_{1h}}$ ($<-6\%\ h^{-1}$) along and west of the high Sierra. Based on trajectory paths (Figs. 3a–c), these areas of negative $\overline{\Delta qv_{1h}}$ lie upstream of high topographical barriers, where blocking, flow deceleration, and water vapor depletion from precipitation are common. Inland- and, particularly, interior-penetrating 950-hPa AR trajectories exhibit positive $\overline{\Delta qv_{1h}}$ downstream of the Canadian Coast

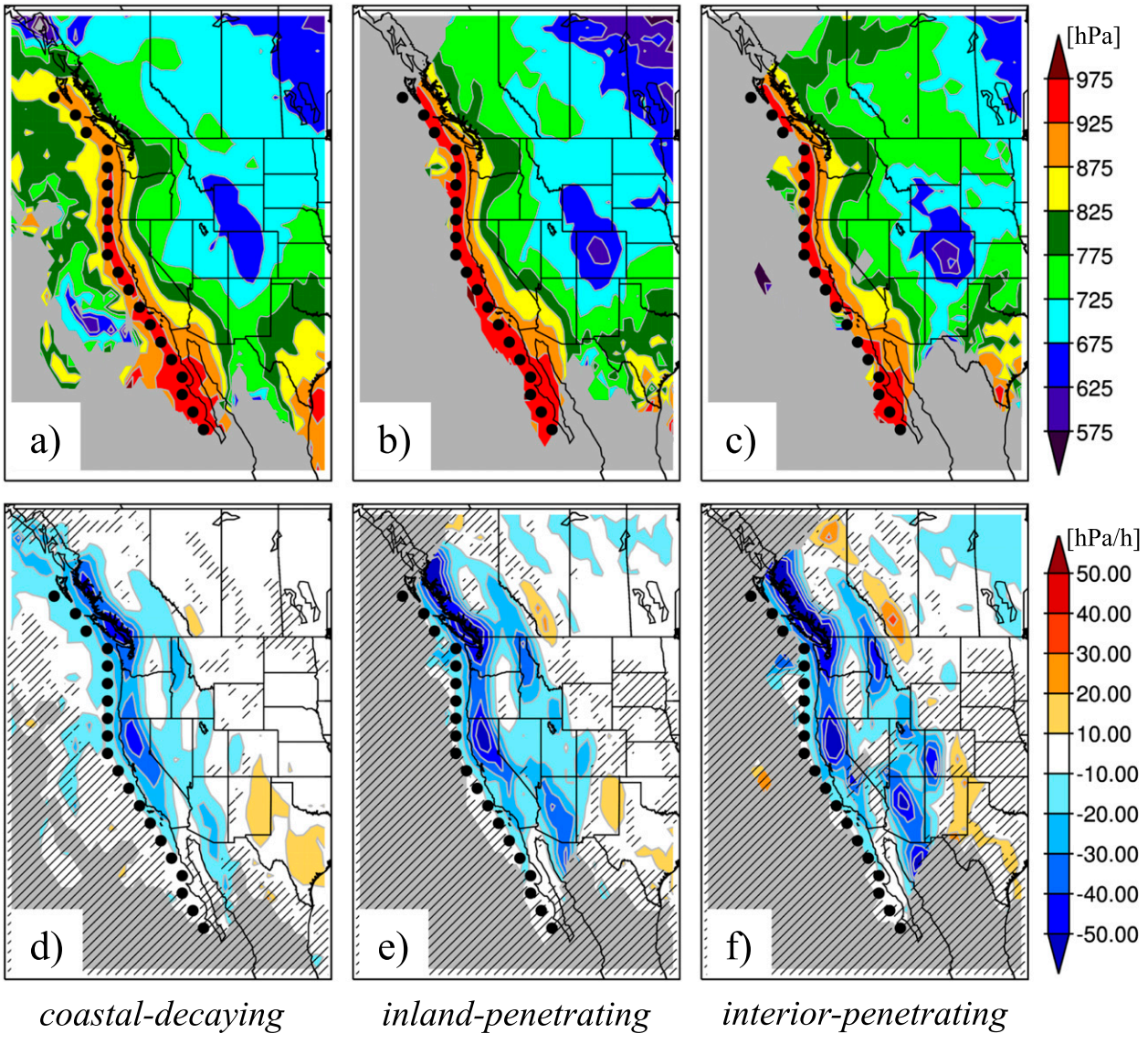

FIG. 9. (a)–(c) Spatial analysis of mean pressure ($\overline{p}$) for (a) coastal-decaying, (b) inland-penetrating, and (c) interior-penetrating 950-hPa AR trajectories. (d)–(f) As in (a)–(c), but for the 1-h mean tendency of pressure, $\overline{\Delta p_{1h}}$. Black circles indicate T_1 grid points. Gray shading indicates no data and stippling indicates that results are not significant at the 95% confidence level following the Student's t test.

Mountains (2%–8% h^{-1}), the southern Cascades, and northern Sierra Nevada (2%–6% h^{-1}), as well as over portions of the Baja Peninsula (2%–8% h^{-1}).

The mean net relative water vapor flux change ($\overline{\Delta q v_{net}}$) along 950-hPa AR trajectories becomes more strongly negative (or less positive) from the coast to the interior, particularly for coastal-decaying 950-hPa AR trajectories (Figs. 11d–f). In contrast, for inland- and interior-penetrating 950-hPa AR trajectories, $\overline{\Delta q v_{net}}$ is strongly positive (>75%) over the Baja Peninsula and parts of the southwestern United States.

Along the coast, the mean 1-h relative q change ($\overline{\Delta q_{1h}}$) of 950-hPa AR trajectories is strongly negative (<−10% h^{-1}) north of the Olympic Peninsula and less negative farther south, similar to the spatial pattern of $\overline{\Delta q v_{1h}}$ (Figs. 12a–c). The term $\overline{\Delta q_{1h}}$ is also substantially negative (−4% h^{-1}) over the Pacific Ranges, particularly over Northern California (<−8% h^{-1}), and, for coastal-decaying AR trajectories, the Sierra Nevada. However, these are areas where $\overline{\Delta q v_{1h}}$ is weakly negative or even positive, suggesting that increases in wind speed over these barriers compensates for decreases in water vapor flux due to water vapor depletion. Over the interior, $\overline{\Delta q_{1h}}$ is most strongly negative along and west of the Idaho–Montana border (<−8% h^{-1}), and for inland- and interior-penetrating AR trajectories, over western

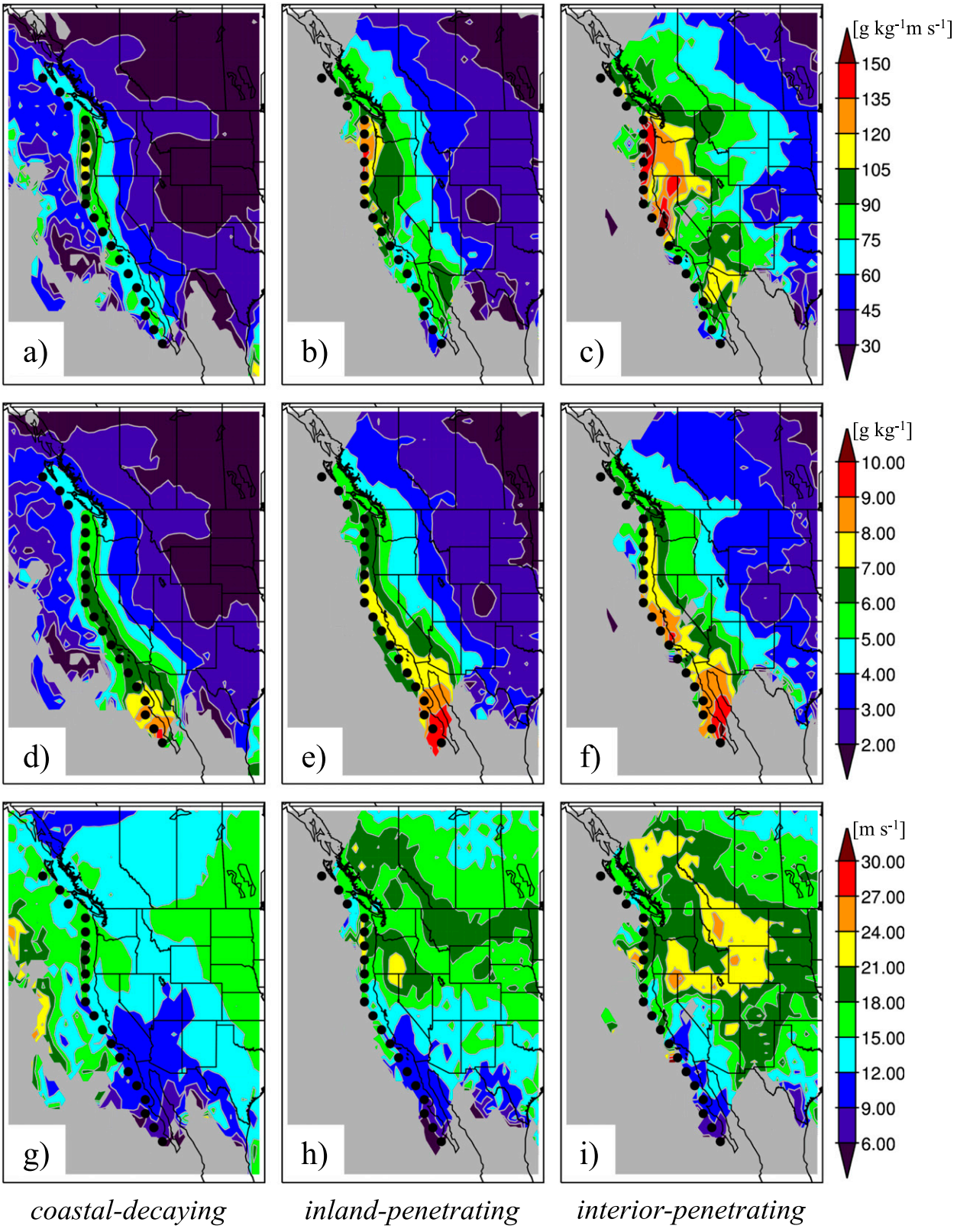

FIG. 10. (a)–(c) Spatial analysis of $\overline{qv}$ for (a) coastal-decaying, (b) inland-penetrating, and (c) interior-penetrating 950-hPa AR trajectories. (d)–(f) As in (a)–(c), but for $\overline{q}$. (g)–(i) As in (a)–(c), but for $\overline{v}$. Black circles indicate T_1 grid points. Gray shading indicates no data.

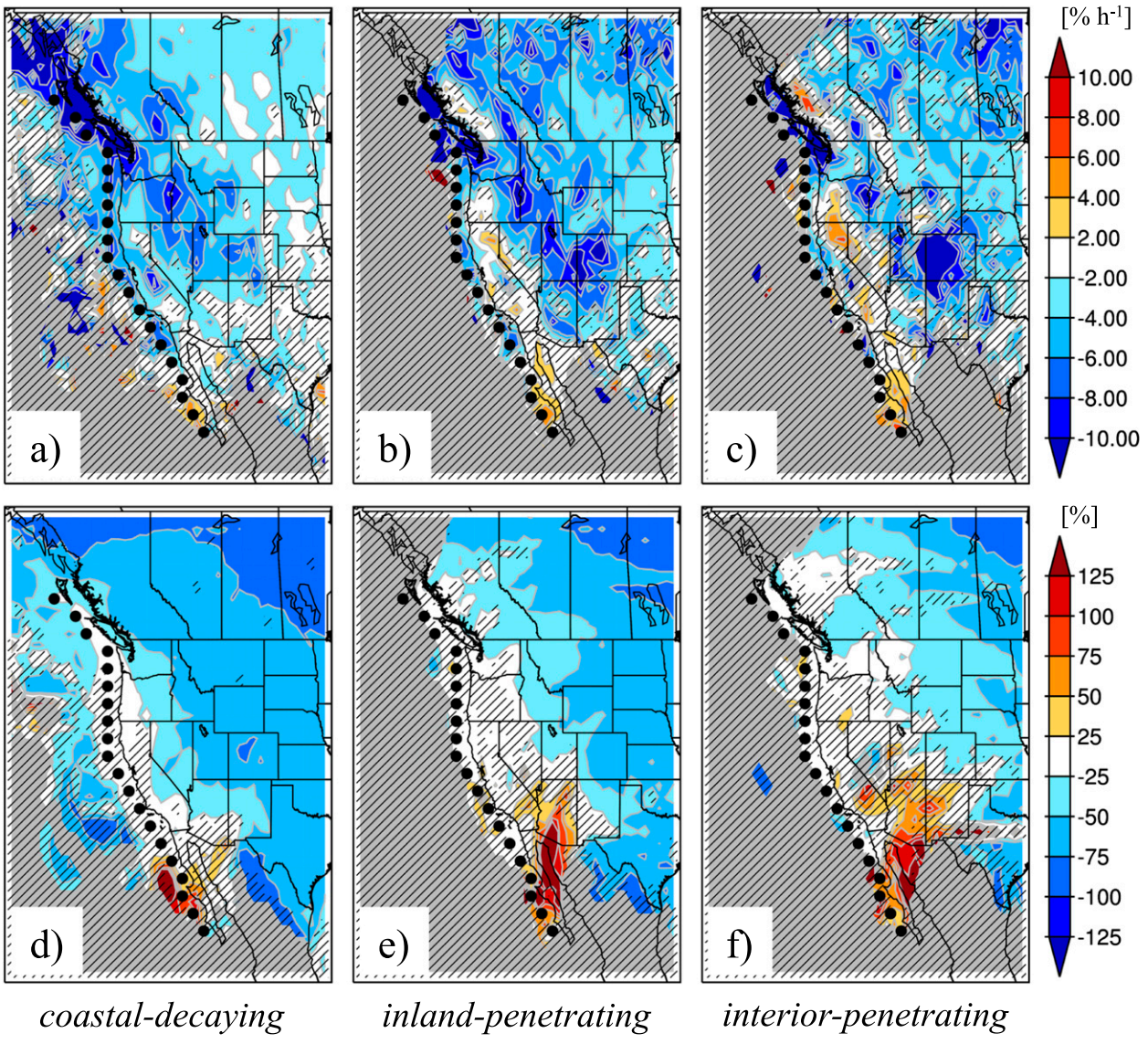

FIG. 11. (a)–(c) Spatial analysis of $\overline{\Delta q v_{1h}}$ for (a) coastal-decaying, (b) inland-penetrating, and (c) interior-penetrating 950-hPa AR trajectories, expressed as a percentage change. (d)–(f) As in (a)–(c), but for $\overline{\Delta q v_{net}}$, integrated over time from trajectory initiation. Black circles indicate T_1 grid points. Gray shading indicates no data and stippling indicates that results are not significant at the 95% confidence level following the Student's *t* test.

Colorado ($<-8\%\,h^{-1}$) and along the Mogollon Rim ($<-6\%\,h^{-1}$). Most of these areas lie over and upstream of high topographical barriers.

The mean net relative q change ($\overline{\Delta q_{net}}$) along 950-hPa AR trajectories becomes more strongly negative from the coast to the interior and generally does so most rapidly for coastal-decaying 950-hPa AR trajectories, similar to $\overline{\Delta q v_{net}}$ (Figs. 12d–f). In contrast to $\overline{\Delta q v_{net}}$, there is no positive $\overline{\Delta q_{net}}$ over the southwestern United States, although for inland- and interior-penetrating AR trajectories, less negative values are found upstream of the Mogollon Rim. Interestingly, the magnitude of water vapor depletion for all AR trajectories is very similar (not shown explicitly), and since inland- and interior-penetrating AR trajectories typically feature larger q at landfall, the result is smaller fractional losses of water vapor for these trajectories. The term $\overline{\Delta q_{net}}$ is analogous to the drying ratio defined by Smith et al. (2005), but with the opposite sign (a positive drying ratio indicates a decrease in $\overline{q}$). Previous work by Smith et al. (2005) and Didlake (2007) found drying ratios of 32% and 43% for air masses crossing Northern California (including both the Coastal Ranges and Sierra Nevada) and the Oregon Cascades, respectively. We find a slightly

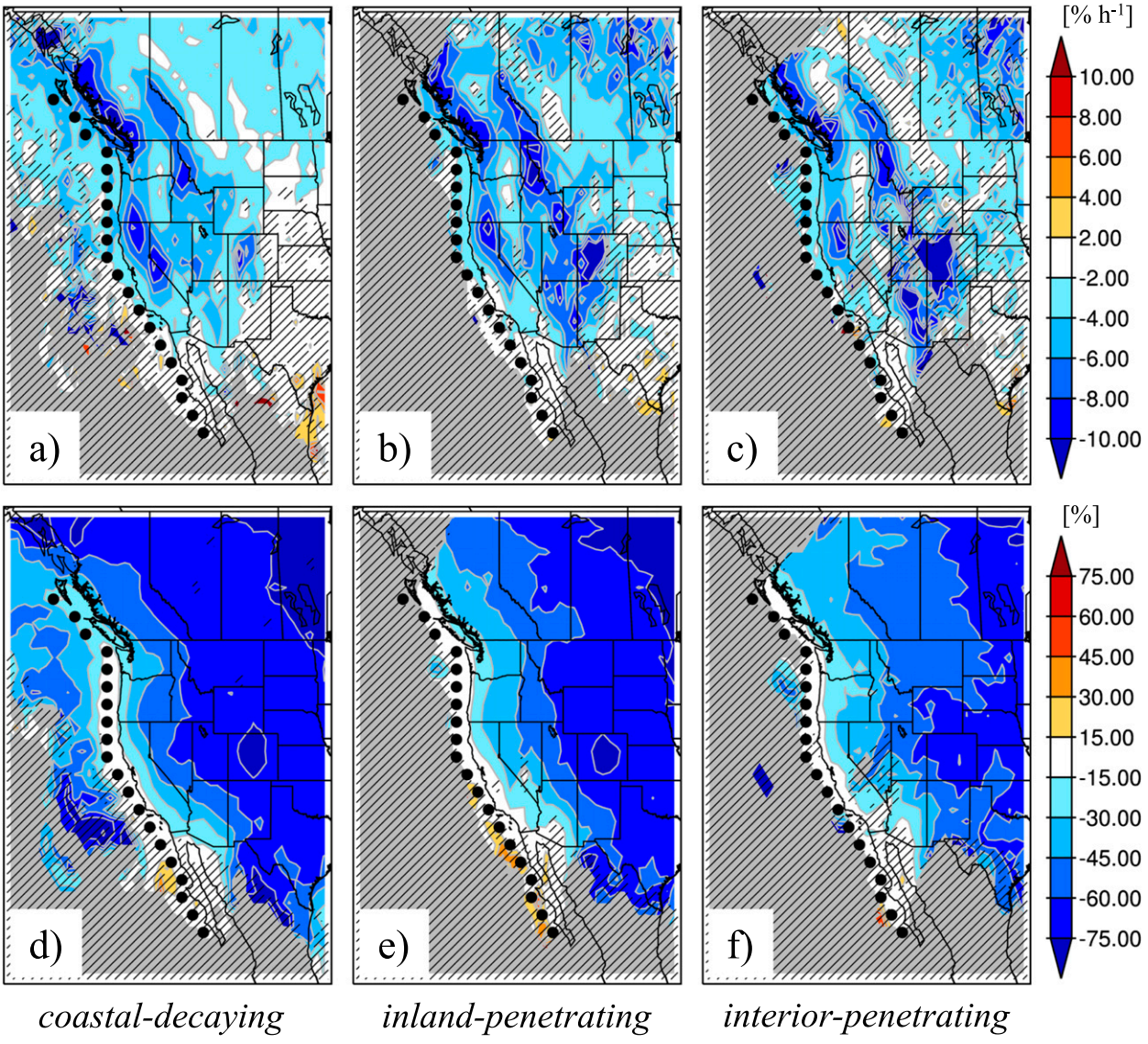

FIG. 12. (a)–(c) Spatial analysis of $\overline{\Delta q_{1h}}$ for (a) coastal-decaying, (b) inland-penetrating, and (c) interior-penetrating 950-hPa AR trajectories, expressed as a percentage change. (d)–(f) As in (a)–(c), but for $\overline{\Delta q_{net}}$, integrated over time from trajectory initiation. Black circles indicate T_1 grid points. Gray shading indicates no data and stippling indicates that results are not significant at the 95% confidence level following the Student's *t* test.

higher ratio (~45%) east of these ranges for coastal-decaying 950-hPa AR trajectories and a lower ratio (~30%–35%) for inland- and interior-penetrating AR trajectories. Considering that the former comprises the majority of events, our findings are in close agreement with prior results.

The mean 1-h relative v change ($\overline{\Delta v_{1h}}$) for 950-hPa AR trajectories is negative from the Canadian coast southward to the Olympic Peninsula and over eastern Oregon, whereas it is positive over the Canadian Coast Mountains, northwestern Montana, Northern California, the Oregon Cascades, and over/downstream of the Mogollon Rim (Figs. 13a–c). These changes in v are generally smallest for coastal-decaying AR trajectories and largest for interior-penetrating AR trajectories. The largest increases in v (>6% h^{-1}) occur over and immediately downstream of major topographical barriers such as the Canadian Coast Mountains, the mountains of northern Idaho and northwestern Montana, the southern Cascades, the northern Sierra, and the Mogollon Rim. Hence, increases in v are often located immediately downstream of decreases in water vapor, both of which are centered on decreases in pressure (increases in altitude; cf. Figs. 9a–c, 12a–c, and 13a–c).

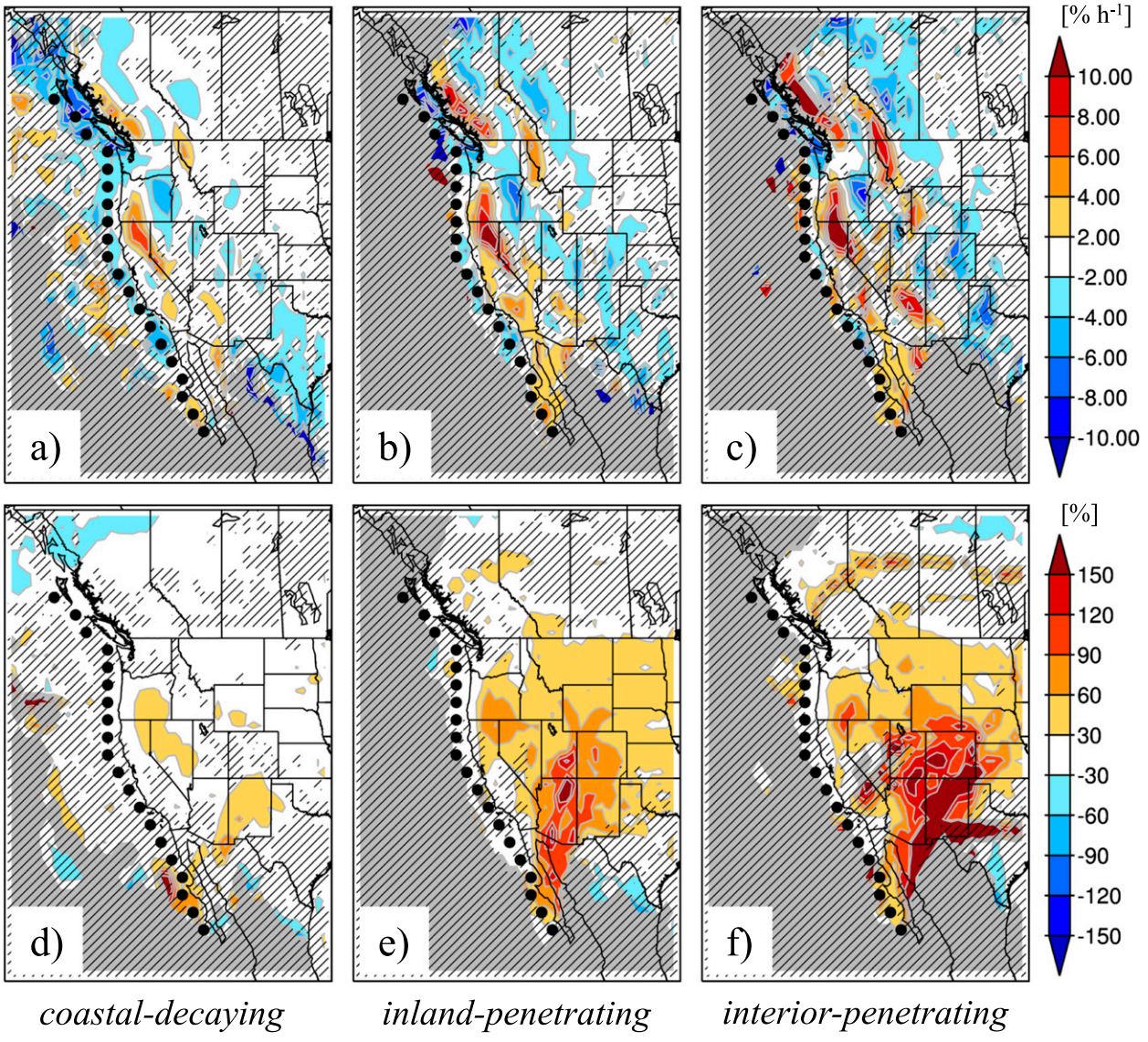

FIG. 13. (a)–(c) Spatial analysis of $\overline{\Delta v_{1h}}$ for (a) coastal-decaying, (b) inland-penetrating, and (c) interior-penetrating 950-hPa AR trajectories, expressed as a percentage change. (d)–(f) As in (a)–(c), but for $\overline{\Delta v_{net}}$, integrated over time from trajectory initiation. Black circles indicate T_1 grid points. Gray shading indicates no data and stippling indicates that results are not significant at the 95% confidence level following the Student's *t* test.

The mean net relative v change ($\overline{\Delta v_{net}}$) along 950-hPa AR trajectories is most strongly positive over the southwestern United States, particularly for those that are inland or interior penetrating (Figs. 13d–f). For these, $\overline{\Delta v_{net}}$ exceeds 60% and 120%, respectively, from the Gulf of California northeastward toward the Colorado Plateau and southern Rocky Mountains. In addition, $\overline{\Delta v_{net}}$ exceeds 60% for inland- and interior-penetrating AR trajectories east of the southern Cascades and northern Sierra Nevada. In contrast, the $\overline{\Delta v_{net}}$ of coastal-decaying AR trajectories does not exceed 30% anywhere over the western United States. There are, in the mean, no regions that feature negative $\overline{\Delta v_{net}}$, which is not surprising given that most trajectories rise substantially from 950 hPa. The larger increases in v over the southwest (relative to the northwest) United States likely result from trajectories with much lower initial v moving northward into areas of stronger v associated with AR-related frontal zones, as well as increases in elevation (cf. Figs. 3a–c and 10g–i).

Mean 1-h and net relative changes in qv, q, and v along the 700-hPa AR trajectories (not shown) reflect many of the geographic and topographic effects described above, with a few exceptions. Despite 700- and 950-hPa AR trajectories featuring comparable values of $\overline{\Delta q_{1h}}$ over

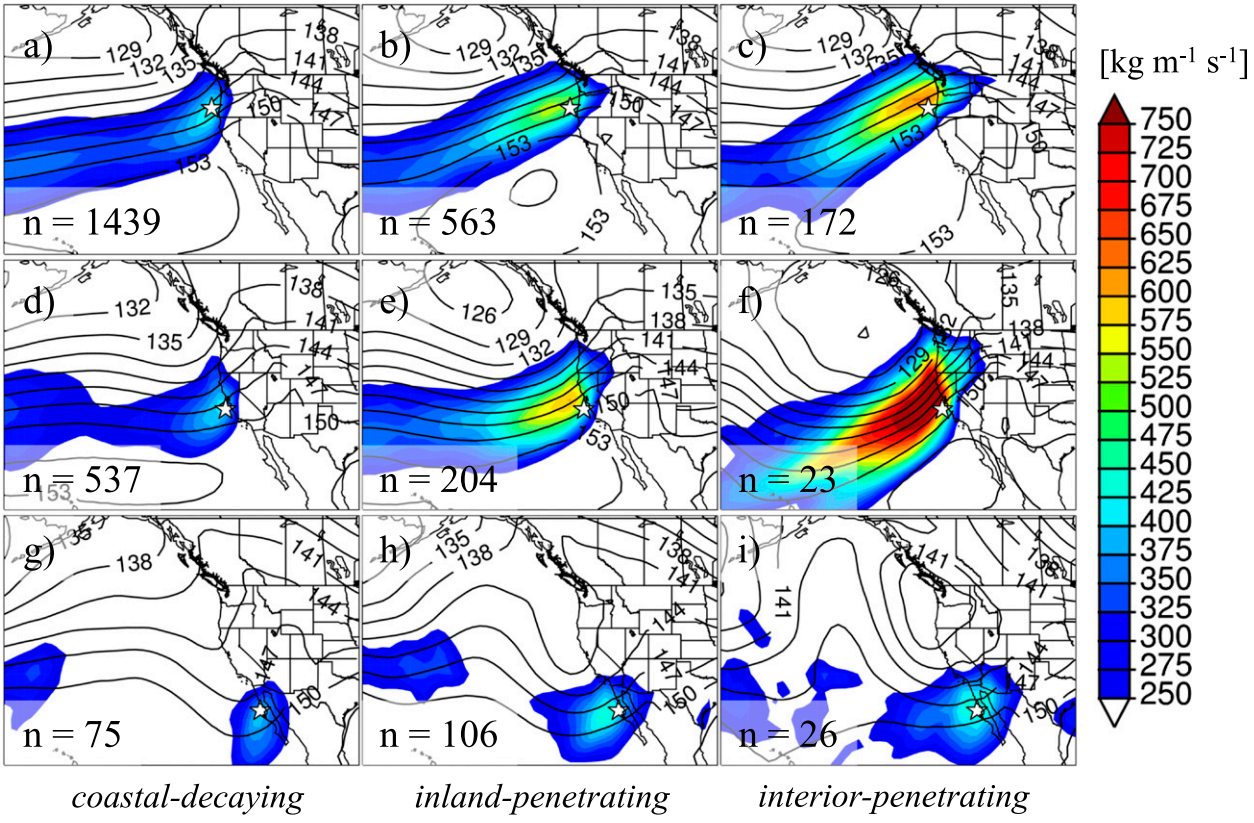

FIG. 14. (a)–(c) Composite of 500-hPa geopotential heights (contours) and integrated water vapor flux (color shading) at the time of initiation for (a) coastal-decaying, (b) inland-penetrating, and (c) interior-penetrating AR trajectories from point 7 (starred location). Number of observations *n* contributing to each composite shown in bottom left. (d)–(f) As in (a)–(c), but for point 12. (g)–(i) As in (a)–(c), but for point 17.

many regions, $\overline{\Delta q_{\text{net}}}$ is much smaller along the former. The term $\overline{\Delta v_{1\text{h}}}$ is also generally smaller along 700-hPa AR trajectories because these begin near the crest level of many western U.S. mountain ranges and experience weaker net orographic lift (to higher levels with greater v) than occurs along 950-hPa AR trajectories.

In summary, changes in water vapor flux along AR trajectories over western North America are strongly influenced by water vapor depletion and changes in wind speed, both typically occurring in the vicinity of large topographic barriers. In most cases, water vapor depletion due to precipitation near and over the Pacific Ranges acts to reduce water vapor flux and induce AR decay. However, in some cases, water vapor depletion is offset by increases in wind speed, which acts to maintain strong water vapor fluxes into the interior, especially over the southwest United States.

7. Synoptic composites

Composites of 850-hPa geopotential height and IVT highlight key differences in the large-scale flow at the time of, and 24 h after, the initiation of coastal-decaying, inland-, and interior-penetrating 950-hPa AR trajectories. The 850-hPa level represents a compromise between low-level trajectory altitudes at initiation (950 hPa) and midlevel trajectory altitudes following penetration into the interior (generally at or above 850 hPa; see Fig. 9). We concentrate on three points along T_1. Point 7 features the largest number of landfalling AR trajectories and lies within the primary pathway for penetration into the northwest interior (Figs. 3 and 5). Point 12 lies west of the high Sierra, features the largest difference in the median qv of coastal-decaying and interior-penetrating AR trajectories (Fig. 6a), and the smallest fraction of the latter (Fig. 5a). Finally, point 17 is considered somewhat characteristic of T_1 grid points along the coast of the Baja Peninsula, although we note the relatively small number of AR trajectories initiated here.

At the time of trajectory initiation (i.e., AR landfall), composites for point 7 feature a trough over the Gulf of Alaska, a ridge over the interior western United States, and an elongated region of IVT $\geq 250\,\text{kg}\,\text{m}^{-1}\,\text{s}^{-1}$ extending across the northeastern Pacific (Figs. 14a–c). Compared to coastal-decaying AR trajectories, inland- and

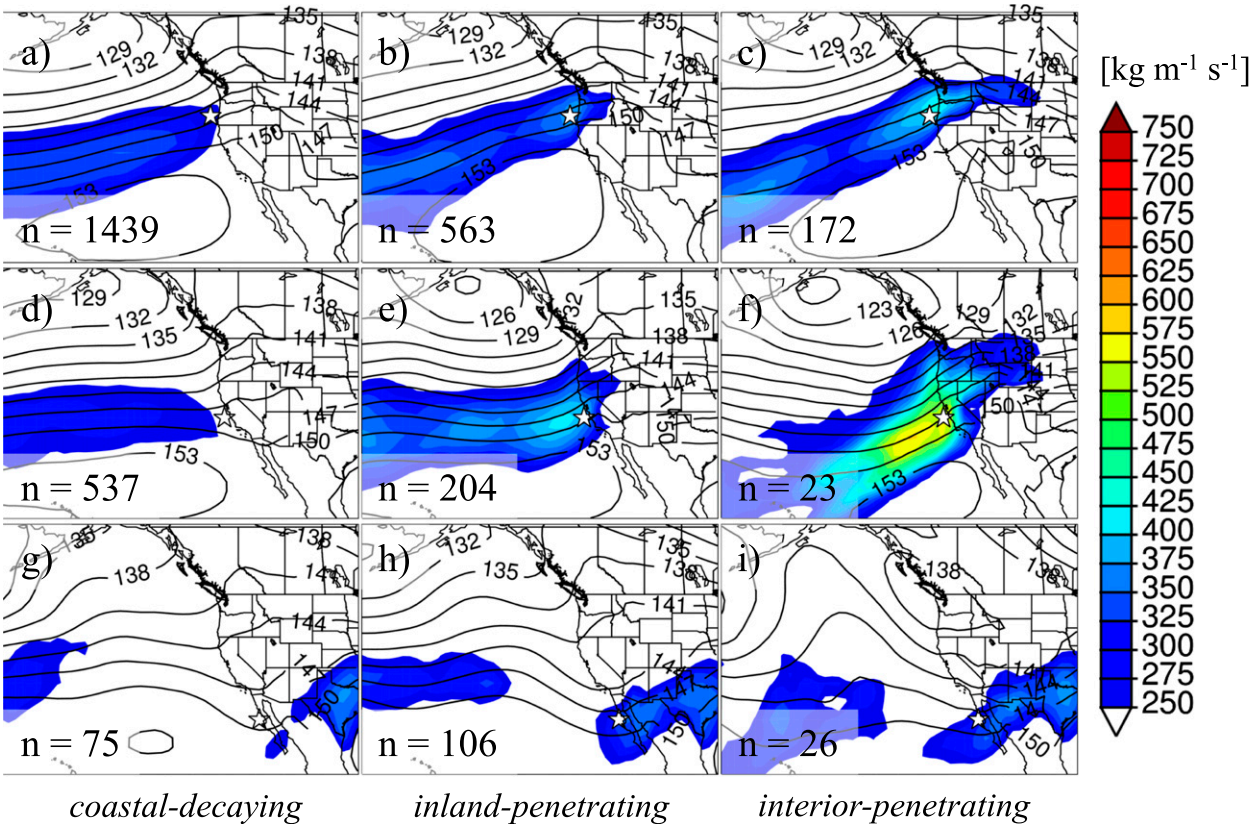

FIG. 15. As in Fig. 14, but for 24 h after initiation.

interior-penetrating AR trajectories feature a more amplified pattern and a stronger ridge, leading to more southwesterly versus westerly oriented flow and larger IVT.

Composites for point 12 feature similar large-scale patterns, but a deeper large-scale trough/cyclone over the Gulf of Alaska (Figs. 14d–f). The ridge is also displaced equatorward, allowing for strong southwesterly flow to impinge on California. As found in the composites for point 7, the pattern is more amplified for inland-and interior-penetrating AR trajectories compared to coastal-decaying AR trajectories, leading to stronger southwesterly flow and greater IVT. Given the rarity of AR penetration over the high Sierra, the IVT of interior-penetrating AR trajectories upstream of this range is especially strong ($\geq$750 kg m^{-1} s^{-1}), as expected from Fig. 6a.

As noted by Rutz et al. (2014), different synoptic patterns enable AR penetration around the northern and southern ends of the Sierra Nevada, and the latter is reflected in the composites for point 17, which feature a trough along the Pacific coast (Figs. 14g–i). Compared to coastal-decaying AR trajectories, inland- and interior-penetrating AR trajectories are associated with a deeper trough, stronger geostrophic flow, and stronger IVT, with a cyclone centered along the northwestern U.S. coast in the case of the latter. Although these ARs can produce significant precipitation (Neiman et al. 2013; Rivera et al. 2014; Rutz et al. 2014) and may feature relatively high q, weaker v generally leads to smaller IVT than found with ARs making landfall farther north.

At 24 h after trajectory initiation, composites for point 7 reveal a stationary, but less-amplified flow pattern for all AR trajectory types (Figs. 15a–c). IVT has generally decreased, but the composite for interior-penetrating AR trajectories features a filament of AR-level IVT (i.e., $\geq$250 kg m^{-1} s^{-1}) that extends across the continental divide into the northern Great Plains. Although the synoptic patterns are similar for all three AR trajectory categories, the ridge over the northwestern United States is modestly stronger in the interior-penetrating AR trajectory composite, leading to stronger geostrophic flow. Similarly, composites for point 12 reveal a stationary, but less amplified pattern for all trajectory types (Figs. 15d–f). Nevertheless, the ridge–trough couplet in the interior-penetrating AR trajectory composite remains strong enough for a broad region of AR-level IVT to penetrate across the northwestern United States and continental divide and into the northern Great Plains.

Composites for point 17 also indicate a deamplified pattern and weakened IVT, but the 850-hPa trough previously centered off the coast of California and the Baja Peninsula has progressed eastward into the southwestern United States and northern Mexico. Composites for the inland- and interior-penetrating AR trajectories show a stronger connection with the Pacific Ocean (i.e., IVT $\geq 250\,\mathrm{kg\,m^{-1}\,s^{-1}}$ extends to the west of the Baja Peninsula), but in all three cases, AR-level IVT is found farther east, likely due to the influence of the Gulf of Mexico.

8. AR regimes

The findings of this study and previous work by Rutz et al. (2014) can be summarized in terms of three geographic regimes for AR penetration into interior western North America (Fig. 16). Regime 1 consists of ARs making landfall on the Pacific coast north of Cape Mendocino (~40.5°N) and comprises the majority (~68%) of trajectories analyzed. Most trajectories within this regime experience moderate amounts of water vapor depletion over the Pacific Ranges and turn anticyclonically as they penetrate into and across the interior. The most frequent pathways for penetration into the interior are found north of the Canadian Coast Mountains and across the Columbia basin and lower terrain of the northern Rocky Mountains near the U.S.–Canada border. Over the United States, this regime is characterized by a relatively high AR frequency, mean duration, and fraction of precipitation attributable to ARs [AR fraction (Rutz et al. 2014)].

Regime 2 consists of ARs making landfall south of Cape Mendocino and north of the U.S.–Mexico border (~32.5°–40.5°N). Within this regime, inland- and interior-penetrating AR trajectories typically follow either an anticyclonic path traversing the relatively low crest of the Cascade–Sierra ranges north of Lake Tahoe, or, less commonly, a cyclonic path south of the high Sierra. In contrast, inland- and interior-penetrating AR trajectories rarely pass over the high Sierra, as flow blocking and water vapor depletion over and upstream of this range frequently lead to AR decay. West of the Sierra, this regime is characterized by decreasing AR frequency from north to south, with AR duration and AR fraction decreasing from the coast to the interior. The AR frequency, duration, and fraction are very small over the Great Basin east of the high Sierra.

Finally, regime 3 consists of ARs making landfall south of the U.S.–Mexico border (~34.5°N) along the Baja Peninsula. The largest fraction of landfalling ARs that penetrate inland and into the interior are found over this region. Within this regime, inland- and interior-penetrating AR trajectories move northeastward into the southwestern United States, often exhibiting weak cyclonic (anticyclonic) curvature farther northwest (southeast). Although trajectories within this regime typically have smaller water vapor fluxes near the coast than those farther north, most experience limited amounts of water vapor depletion over the mountains of Southern California and the Baja Peninsula (some experience increases over the Gulf of California) and nearly half remain AR related when they reach the lower Colorado River basin. South and west of the Mogollon Rim, this regime is characterized by small AR frequency, relatively large mean duration, and large AR fraction. Over and downstream of the Mogollon Rim, across the Colorado Plateau, these quantities decrease rapidly, particularly the AR duration and fraction.

9. Summary

We have used trajectories released at 950 and 700 hPa within cool-season ARs along the Pacific coast to better understand the processes contributing to AR maintenance and decay over western North America and the factors that contribute to AR penetration into the western interior. These trajectories were classified as coastal-decaying, inland-, or interior-penetrating, based on whether or not they remain within an AR at selected transects over western North America. The largest number of inland- and interior-penetrating AR trajectories make landfall north of Cape Mendocino (~40.5°N). These often follow relatively low-elevation corridors, such as north of the Canadian Coast Mountains or through the Columbia River basin, into the interior. The AR trajectories making landfall south of Cape Mendocino and north of the U.S.–Mexico border (~34.5°N) are more likely to become inland- or interior-penetrating AR trajectories if they move either north or south of the high Sierra, whereas those passing directly over this range are typically associated with AR decay. Finally, although few AR trajectories make landfall along the Baja Peninsula, these trajectories are the most likely to remain within an AR as they penetrate into the interior.

At initiation, interior-penetrating AR trajectories are characterized by larger water vapor transport than coastal-decaying AR trajectories, especially west of the high Sierra. This difference is partially attributable to larger specific humidities for 950-hPa AR trajectories and larger initial wind speeds for 700-hPa AR trajectories. Additionally, interior-penetrating AR trajectories are typically associated with a more amplified 850-hPa flow pattern over the northeastern Pacific and western United States, more southwesterly (vs westerly) flow,

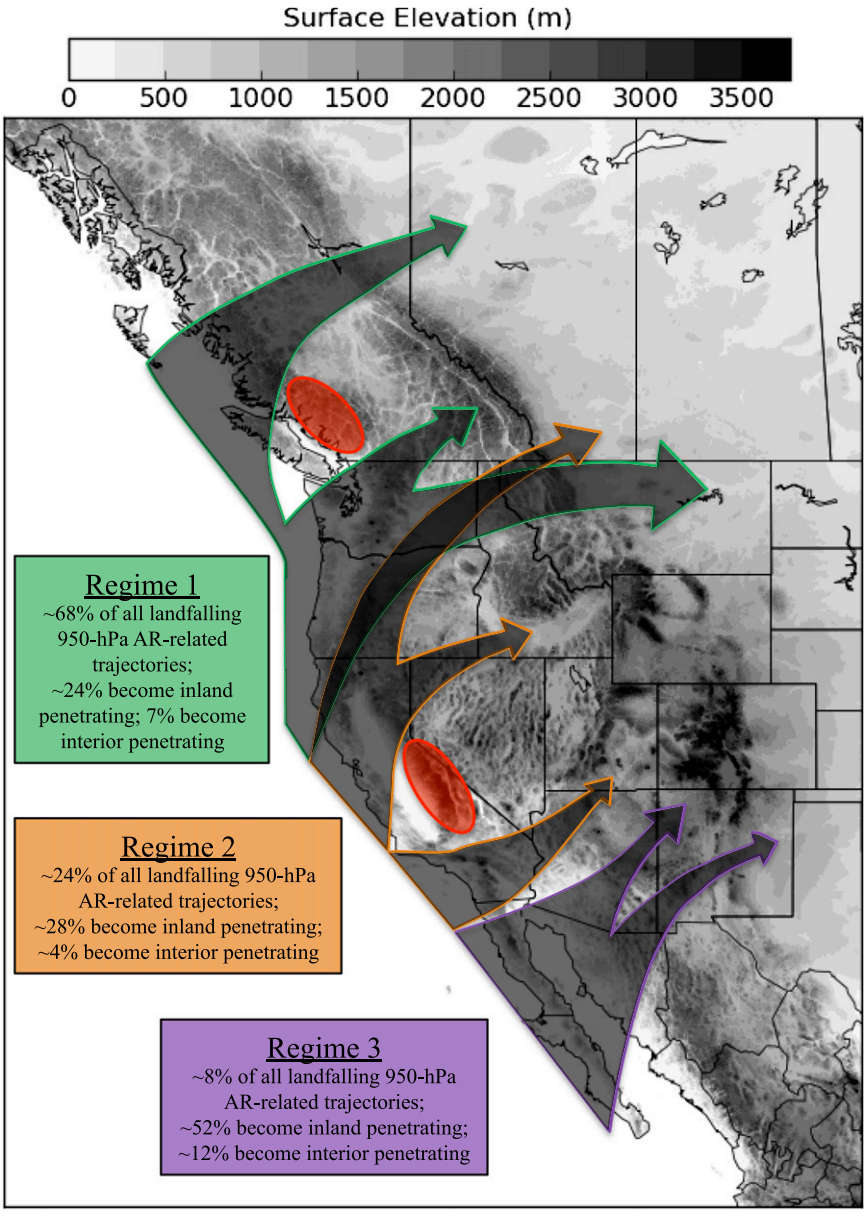

FIG. 16. Schematic showing the primary pathways for the penetration of 950-hPa AR-related trajectories into the interior of western North America. Pathways associated with regimes 1–3 are represented by green, orange, and purple arrows, respectively. Regions associated with frequent AR decay are shaded in red. Topography is shaded in grayscale. Note that while this schematic highlights common regimes and pathways, individual trajectories follow many different paths.

and higher values of vertically integrated water vapor transport (IVT).

Changes in water vapor flux along AR-related trajectories over western North America are strongly influenced by water vapor depletion and changes in wind speed, both typically occurring in the vicinity of large topographic barriers such as the Canadian Coast Mountains, the northern U.S. Rockies, the northern Sierra, and the Mogollon Rim. In most cases, water vapor depletion due to orographic precipitation along the Pacific Ranges reduces water vapor flux and induces AR decay. However, increases in wind speed along trajectories can act to offset decreases in water vapor and maintain strong water vapor fluxes over the interior, especially over the southwestern United States. Additionally, interior-penetrating AR trajectories over the southwestern United States are

typically associated with an approaching 850-hPa trough or cyclone. Increases in wind speed are generally less pronounced for AR trajectories over the northwestern United States, but so are decreases in water vapor, and the intensity of landfalling ARs also contributes to the maintenance of relatively strong water vapor fluxes over the northwest interior.

Additional work is needed to more fully understand the inland penetration of ARs over western North America. Our results suggest that large values of low-level (950 hPa) specific humidity and midlevel (700 hPa) wind speed near landfall are indicative of inland- or interior-penetrating ARs, but having examined only two levels, it is not clear how the vertical distribution of these characteristics at landfall ultimately affect their distribution over the interior. Future work might involve a statistical assessment of how strongly the initial specific humidity and wind speed affect eventual AR maintenance over the interior. Furthermore, the 1.5° reanalysis does not adequately resolve the complex topography of western North America (Fig. 1), making it difficult to fully quantify water vapor flux tendencies along AR trajectories. Finally, other factors not examined here, such as stability, flow direction, and convective processes not captured by our trajectories, likely play a role in AR penetration into the interior and warrant further investigation.

Acknowledgments. We thank Mike Dettinger for conversations that helped to clarify the text. Reviews by Jay Cordeira and one anonymous reviewer also improved the manuscript. We also gratefully acknowledge the provision of datasets, software, and/or computer time provided by the European Centre for Medium-Range Weather Forecasts and the University of Utah Center for High Performance Computing. This article is based on research supported by a series of grants from the NOAA/NWS CSTAR program. Any opinions, findings, and conclusions or recommendations expressed herein are those of the authors and do not necessarily reflect those of the NOAA/NWS.

REFERENCES

Bernhardt, D., 2006: Glacier National Park flooding November 2006. NWS Western Region Tech. Attachment 08-23, 15 pp. [Available online at http://www.wrh.noaa.gov/media/wrh/online_publications/talite/talite0823.pdf.]

Berrisford, P., D. Dee, K. Fielding, M. Fuentes, P. Kallberg, S. Kobayashi, and S. Uppala, 2009: The ERA-Interim archive. ECMWF Tech. Rep. 1, 16 pp. [Available online at http://old.ecmwf.int/publications/library/do/references/show?id=89203.]

Cordeira, J. M., F. M. Ralph, and B. J. Moore, 2013: The development and evolution of two atmospheric river events in proximity to western North Pacific tropical cyclones in October 2010. *Mon. Wea. Rev.,* **141,** 4234–4255, doi:10.1175/MWR-D-13-00019.1.

Dee, D. P., and Coauthors, 2011: The ERA-Interim Reanalysis: Configuration and performance of the data assimilation system. *Quart. J. Roy. Meteor. Soc.,* **137,** 553–597, doi:10.1002/qj.828.

Dettinger, M. D., F. M. Ralph, T. Das, P. J. Neiman, and D. R. Cayan, 2011: Atmospheric rivers, floods, and the water resources of California. *Water,* **3,** 445–478, doi:10.3390/w3020445.

Didlake, A. C., Jr., 2007: An analysis of water vapor flux and orographic precipitation in northern California. B.S. thesis, Dept. of Geology and Geophysics, Yale University, 47 pp.

Hughes, M., K. M. Mahoney, P. J. Neiman, B. J. Moore, M. Alexander, and F. M. Ralph, 2014: The landfall and inland penetration of a flood-producing atmospheric river in Arizona. Part II: Sensitivity of modeled precipitation to terrain height and atmospheric river orientation. *J. Hydrometeor.,* **15,** 1954–1974, doi:10.1175/JHM-D-13-0176.1.

Kanamitsu, M., 1989: Description of the NMC Global Data Assimilation and Forecast System. *Wea. Forecasting,* **4,** 335–342, doi:10.1175/1520-0434(1989)004<0335:DOTNGD>2.0.CO;2.

Knippertz, P., and J. E. Martin, 2007: A Pacific moisture conveyor belt and its relationship to a significant precipitation event in the semiarid southwestern United States. *Wea. Forecasting,* **22,** 125–144, doi:10.1175/WAF963.1.

——, and H. Wernli, 2010: A Lagrangian climatology of tropical moisture exports to the Northern Hemispheric extratropics. *J. Climate,* **23,** 987–1003, doi:10.1175/2009JCLI3333.1.

——, ——, and G. Gläser, 2013: A global climatology of tropical moisture exports. *J. Climate,* **26,** 3031–3045, doi:10.1175/JCLI-D-12-00401.1.

Lackmann, G. M., J. R. Gyakum, and R. Benoit, 1998: Moisture transport diagnosis of a wintertime precipitation event in the Mackenzie River basin. *Mon. Wea. Rev.,* **126,** 668–692, doi:10.1175/1520-0493(1998)126<0668:MTDOAW>2.0.CO;2.

Lavers, D. A., R. P. Allan, E. F. Wood, G. Villarini, D. J. Brayshaw, and A. J. Wade, 2011: Winter floods in Britain are connected to atmospheric rivers. *Geophys. Res. Lett.,* **38,** L23803, doi:10.1029/2011GL049783.

Moore, B. J., P. J. Neiman, F. M. Ralph, and F. Barthold, 2012: Physical processes associated with heavy flooding rainfall in Nashville, Tennessee, and vicinity during 1–2 May 2010: The role of an atmospheric river and mesoscale convective systems. *Mon. Wea. Rev.,* **140,** 358–378, doi:10.1175/MWR-D-11-00126.1.

Neiman, P. J., F. M. Ralph, A. B. White, D. E. Kingsmill, and P. O. G. Persson, 2002: The statistical relationship between upslope flow and rainfall in California's Coastal Mountains: Observations during CALJET. *Mon. Wea. Rev.,* **130,** 1468–1492, doi:10.1175/1520-0493(2002)130<1468:TSRBUF>2.0.CO;2.

——, ——, G. A. Wick, Y.-H. Kuo, T.-K. Wee, Z. Ma, G. H. Taylor, and M. D. Dettinger, 2008: Diagnosis of an intense atmospheric river impacting the Pacific Northwest: Storm summary and offshore vertical structure observed with COSMIC satellite retrievals. *Mon. Wea. Rev.,* **136,** 4398–4420, doi:10.1175/2008MWR2550.1.

——, L. J. Schick, F. M. Ralph, M. Hughes, and G. A. Wick, 2011: Flooding in western Washington: The connection to atmospheric rivers. *J. Hydrometeor.,* **12,** 1337–1358, doi:10.1175/2011JHM1358.1.

——, F. M. Ralph, B. J. Moore, M. Hughes, K. M. Mahoney, J. M. Cordeira, and M. D. Dettinger, 2013: The landfall and inland penetration of a flood-producing atmospheric river in Arizona. Part I: Observed synoptic-scale, orographic, and hydrometeorological characteristics. *J. Hydrometeor.,* **14,** 460–464, doi:10.1175/JHM-D-12-0101.1.

——, ——, ——, and R. J. Zamora, 2014: The regional influence of an intense Sierra barrier jet and landfalling atmospheric river on orographic precipitation in northern California: A case study. *J. Hydrometeor.,* **15,** 1419–1439, doi:10.1175/JHM-D-13-0183.1.

Newell, R. E., and Y. Zhu, 1994: Tropospheric rivers: A one-year record and a possible application to ice core data. *Geophys. Res. Lett.,* **21,** 113–116, doi:10.1029/93GL03113.

——, N. E. Newell, Y. Zhu, and C. Scott, 1992: Tropospheric rivers?—A pilot study. *Geophys. Res. Lett.,* **19,** 2401–2404, doi:10.1029/92GL02916.

Ralph, F. M., P. J. Neiman, and G. A. Wick, 2004: Satellite and CALJET aircraft observations of atmospheric rivers over the eastern North Pacific Ocean during the winter of 1997/98. *Mon. Wea. Rev.,* **132,** 1721–1745, doi:10.1175/1520-0493(2004)132<1721:SACAOO>2.0.CO;2.

——, ——, and R. Rotunno, 2005: Dropsonde observations in low-level jets over the northeastern Pacific Ocean from CALJET-1998 and PACJET-2001: Mean vertical-profile and atmospheric-river characteristics. *Mon. Wea. Rev.,* **133,** 889–910, doi:10.1175/MWR2896.1.

——, ——, G. A. Wick, S. I. Gutman, M. D. Dettinger, D. R. Cayan, and A. B. White, 2006: Flooding on California's Russian River: Role of atmospheric rivers. *Geophys. Res. Lett.,* **33,** L13801, doi:10.1029/2006GL026689.

——, ——, G. N. Kiladis, K. Weickmann, and D. W. Reynolds, 2011: A multiscale observational case study of a Pacific atmospheric river exhibiting tropical–extratropical connections and a mesoscale frontal wave. *Mon. Wea. Rev.,* **139,** 1169–1189, doi:10.1175/2010MWR3596.1.

——, T. Coleman, P. J. Neiman, R. J. Zamora, and M. D. Dettinger, 2013: Observed impacts of duration and seasonality of atmospheric-river landfalls on soil moisture and runoff in coastal northern California. *J. Hydrometeor.,* **14,** 443–459, doi:10.1175/JHM-D-12-076.1.

Rigby, J. G., 1998: The 1997 New Year's floods in western Nevada. Special Publ. 23, Nevada Bureau of Mines and Geology, University of Nevada, Reno, NV, 111 pp.

Rivera, E. R., F. Dominguez, and C. L. Castro, 2014: Atmospheric rivers and cool season extreme precipitation events in the Verde River basin of Arizona. *J. Hydrometeor.,* **15,** 813–829, doi:10.1175/JHM-D-12-0189.1.

Rutz, J. J., and W. J. Steenburgh, 2012: Quantifying the role of atmospheric rivers in the interior western United States. *Atmos. Sci. Lett.,* **13,** 257–251, doi:10.1002/asl.392.

——, ——, and F. M. Ralph, 2014: Climatological characteristics of atmospheric rivers and their inland penetration over the western United States. *Mon. Wea. Rev.,* **142,** 905–921, doi:10.1175/MWR-D-13-00168.1.

Simmons, A., S. Uppala, D. Dee, and S. Kobayashi, 2007: ERA-Interim: New ECMWF reanalysis products from 1989 onwards. *ECMWF Newsletter,* No. 110, ECMWF, Reading, United Kingdom, 25–35.

Smith, R. B., I. Barstad, and L. Bonneau, 2005: Orographic precipitation and Oregon's climate transition. *J. Atmos. Sci.,* **62,** 177–191, doi:10.1175/JAS-3376.1.

Sodemann, H., and A. Stohl, 2013: Moisture origin and meridional transport in atmospheric rivers and their association with multiple cyclones. *Mon. Wea. Rev.,* **141,** 2850–2868, doi:10.1175/MWR-D-12-00256.1.

Stohl, A., C. Forster, and H. Sodemann, 2008: Remote sources of water vapor forming precipitation on the Norwegian west coast at 60°N—A tale of hurricanes and an atmospheric river. *J. Geophys. Res.,* **113,** D05102, doi:10.1029/2007JD009006.

Uppala, S., D. Dee, S. Kobayashi, P. Berrisford, and A. Simmons, 2008: Towards a climate data assimilation system: Status update of ERA-Interim. *ECMWF Newsletter,* No. 115, ECMWF, Reading, United Kingdom, 12–18.

Wernli, H., 1997: A Lagrangian-based analysis of extratropical cyclones. II: A detailed case-study. *Quart. J. Roy. Meteor. Soc.,* **123,** 1677–1706, doi:10.1002/qj.49712354211.

Zhu, Y., and R. E. Newell, 1998: A proposed algorithm for moisture fluxes from atmospheric rivers. *Mon. Wea. Rev.,* **126,** 725–735, doi:10.1175/1520-0493(1998)126<0725:APAFMF>2.0.CO;2.